



## PAPER



Cite this: *J. Mater. Chem. A*, 2022, 10, 632

## *In situ* formation of circular and branched oligomers in a localized high concentration electrolyte at the lithium-metal solid electrolyte interphase: a hybrid *ab initio* and reactive molecular dynamics study†

Yue Liu, Qintao Sun, Peiping Yu, Bingyun Ma, Hao Yang,  Jiayi Zhang, Miao Xie and Tao Cheng \*

Developing advanced electrolytes has been considered as a promising approach to stabilize the lithium (Li) metal anode via the formation of a stable solid electrolyte interphase (SEI) that can protect the Li anode to enable long-term cycling stability in rechargeable Li metal batteries (LMBs). Recently, the concept of localized high-concentration electrolyte (LHCE) is emerging as an efficient state-of-the-art strategy in developing advanced electrolytes for LMBs. However, the underlying reaction mechanism of SEI formation in LHCEs with the Li anode remains far from clear. In this work, a hybrid *ab initio* and reactive molecular dynamics (HAIR) scheme is employed to investigate the detailed reactions of a typical LHCE system that consists of lithium bis(fluorosulfonyl)-imide (LiFSI) in dimethoxyethane (DME) with 1,1,2,2-tetrafluoroethyl-2,2,3,3-tetrafluoropropylether (TTE). The initial reaction involves the release of the fluorine atoms of dilute 1,1,2,2-tetrafluoroethyl-2,2,3,3-tetrafluoropropylether (TTE) initiated by  $\text{Li}^0$  followed by C–O bond cleavages. Polymerization processes are captured in an extended 2.8 ns HAIR simulation, with both circular and branched oligomers identified as the organic part of the SEI layer; meanwhile, the LiF forms a clear inorganic SEI, as confirmed by simulated radial distribution function (RDF) and X-ray photoelectron spectroscopy (XPS). Overall, the simulated results reveal that TTE releases the F to facilitate the formation and enrichment of LiF and provide an unsaturated carbon-chain as the backbone for *in situ* polymerization. Experimentally, these elastic *in situ* oligomers with LiF offer improved SEI performance. These theoretical results depict the basic chemical mechanism between LHCE and the electrode, providing useful information for the development of sophisticated electrolyte systems.

Received 23rd September 2021  
Accepted 4th December 2021

DOI: 10.1039/d1ta08182a

rsc.li/materials-a

Conventional lithium (Li) ion batteries (LIBs) can no longer satisfy the rapid-growing demands for high-energy storage, therefore developing high-energy-density rechargeable batteries has become an urgent need for applications such as electric vehicles, portable devices, grid energy storage, etc.<sup>1–3</sup> Li metal,

with a high specific capacity of  $3860 \text{ mA h g}^{-1}$  and a low electrochemical potential of  $-3.040 \text{ V}$  (vs. standard hydrogen electrode), is an ideal anode to construct the Li-metal battery (LMB) system.<sup>4–6</sup> However, the uncontrollable Li dendrite growth and reduction of electrolytes with Li metal, which imposes low coulombic efficiencies (CEs) and high safety risks for LMBs, significantly impede the further development and practical application of the LMB system.<sup>7–10</sup>

In recent years, one promising method to stabilize the Li-metal anode has been manipulating the solid electrolyte interphase (SEI) layer to protect the Li anode effectively. A robust and stable SEI can serve as a channel for charge and mass transfer across the electrodes and inhibit the dendrite growth as a passivation layer.<sup>11,12</sup> The properties and performance of the SEI layer are significantly determined by its composition and concentration that originate from electrolytes. Strategies that regulate the composition and concentration of electrolytes have

Institute of Functional Nano and Soft Materials (FUNSOM), Soochow University, Suzhou 215123, China. E-mail: tcheng@suda.edu.cn

† Electronic supplementary information (ESI) available: The initial configurations and images of the lithium-metal anode surface and LiFSI/DME/TTE electrolyte are provided in Fig. S1. Snapshots of the Li-metal anode and LiFSI/DME/TTE electrolyte with AIMD are provided in Fig. S2. Oligomers formed from two configurations after 275 ps (50 cycles) using HAIR MD simulation are given in Fig. S3. Radial distribution function and integrated number of bonds for (a) C–C; (b) Li–F for configuration 1, (c) C–C; (d) Li–F for configuration 2 after 2.85 ns HAIR simulations are shown in Fig. S4. XPS spectra, relative molecular weight, and XRD patterns are provided in Fig. S5 and S6. Experimental and theoretical XPS binding energy and relative binding energy shifts are listed in Tables S1–S3. See DOI: 10.1039/d1ta08182a

been developed to control SEI formation.<sup>13–18</sup> Significant progress in developing superior electrolytes has been made by combining experiment and theory for low-temperature applications<sup>18</sup> and improved cycling performance.<sup>26</sup> For example, a high-concentration electrolyte (HCE) with unique physico-chemical properties exhibits outstanding electrochemical performance.<sup>19,20</sup> Qian *et al.*<sup>21</sup> proposed a high-concentration (>4 M) lithium bis(fluorosulfonyl)-imide (LiFSI) in dimethoxyethane (DME) that reaches 99% CE while significantly suppressing the dendrite growth. Such improvement has been attributed to the change in electronic structure as concentration increases. Density functional theory (DFT) calculations show that in HCE, the energy of the lowest unoccupied molecular-orbital (LUMO) of FSI<sup>−</sup> anions decreases, indicating that the FSI<sup>−</sup> is prone to accepting electrons to be reduced. Such sacrificial decomposition regulates the SEI component which increases the stability of LMBs.<sup>22</sup> Therefore, increasing the salt concentration is one straightforward way to improve the performance.

Despite the improved performance, HCE is not ideal because of its high cost, large viscosity, *etc.* Recently, the concept of localized high concentration electrolyte (LHCE) has attracted extensive attention because it solves the problems of HCE while maintaining superior performance.<sup>23–26</sup> The idea of LHCE originates from HCE with the introduction of an extra non-solvating diluent solvent which allows the existence of an inner localized HCE region that retains HC solvation features and an outer solvent with the physical properties of LCE. The LHCE system receives extensive attention because of its superior performance. LiFSI/DME/TTE is an electrolyte that exhibits top performance as reported by Ren *et al.* Meanwhile, according to the existing experimental evidence, TTE significantly changes the solvation structure, which in turn affects the SEI and the performance. As reported by Ren *et al.*, an LHCE system consists of an LiFSI–DME system with 1,1,2,2-tetrafluoroethyl-2,2,3,3-tetrafluoropropylether (TTE) as the diluent, whose performance can reach more than 90% capacity with no retention after 250 cycles and >99% CE in high-voltage Li||NMC811 cells.<sup>17</sup> As confirmed by O-NMR, Li<sup>+</sup> is still in contact with FSI<sup>−</sup> after adding TTE. Further XPS analysis suggests that both FSI<sup>−</sup> and TTE suffer from reductive decomposition which contributes to the SEI formation.<sup>27</sup>

Despite the significant progress in the experiment, the fundamental problems in LHCE, such as the detailed solvation structure and elementary reactions in SEI formation, remain unclear.<sup>28–30</sup> Beltran *et al.*<sup>31</sup> investigated the liquid structure and electronic properties of LiFSI + dimethyl carbonate (DMC) + bis(2,2,2-trifluoroethyl) ether (BTFE), a high performance LHCE, using the first-principles screening methodology. They found that the strongly interacting Li<sup>+</sup>, FSI<sup>−</sup> and DMC developed a complex three-dimensional island-like structure which is not disturbed by BTFE until the concentration decreases to 1.77 M. In another LHCE case, 1 M LiFSI/DME in tris(2,2,2-trifluoroethyl) orthoformate (TFEO) diluent solvent, Zheng *et al.*<sup>32</sup> carried out 20 ps *ab initio* molecular dynamics (AIMD) simulation<sup>33,34</sup> to investigate the initial reactions in SEI formation. They found that both FSI<sup>−</sup> and TFEO can provide F<sup>−</sup> to form the LiF layer considered important in stabilizing the SEI.

Using AIMD, Leung and Budzien investigated the initial decomposition of ethylene carbonate (EC) on a graphitic anode,<sup>33</sup> and Martinez *et al.* studied similar reactions on a Si anode.<sup>34</sup> Bedrov used ReaxFF MD to expand the simulation and look at the long-term response of EC.<sup>39</sup> These computational results offered useful information, but they were hampered owing to AIMD's high cost.

This paper uses a hybrid method, a hybrid *ab initio* and reactive force field dynamics (HAIR), to extend the simulation to nanoseconds. HAIR can extend the AIMD simulation to 10 to 100 times while maintaining DFT accuracy,<sup>35–38</sup> because reactive force field (ReaxFF)<sup>39</sup> can replace the costly AIMD simulation in accelerating mass transfer when the accuracy of ReaxFF can be trained to level up with AIMD. The details of the simulation setup and HAIR method are as follows.

A 6-layer (3 × 3) supercell slab of Li (100) is used with the bottom two layers fixed to model the Li-metal anode with the electrolyte.<sup>40,41</sup> The number of molecules of LiFSI, DME, and diluent solvent TTE are 2, 2, and 5, respectively, close to the experimental molar ratio of 1 : 1 : 3.<sup>27</sup> The size simulation cell is 10.5 × 10.5 × 26.5 Å. Two independent simulation models are selected from 10 randomly generated configurations. The difference between these two cases is, as shown in Fig. S1,† that the LiFSI is close to the Li-metal surface in case 1, while the LiFSI is far from the surface and coordinated with DME and surrounded by TTE in case 2.

After geometry optimization, the AIMD and ReaxFF portions are performed alternately in the HAIR method. AIMD is calculated using Vienna *Ab initio* Simulation Package (VASP 5.4.4),<sup>42</sup> while the ReaxFF MD simulations are conducted using the Large scale Atomic/Molecular Massively Parallel Simulator (LAMMPS 2018) software.<sup>43</sup> A homemade python shell is employed to couple VASP and LAMMPS. The timesteps for AIMD and ReaxFF MD are 1 fs and 0.25 fs. A 10-time factor is used in the first 50 cycles to achieve long-time hybrid simulations, including 0.5 ps AIMD and 5 ps ReaxFF MD for one cycle. Based on the reliable initial reaction process, the following 50 cycles of HAIR simulations are performed with a 100-time factor to accelerate the reaction. All HAIR simulations were conducted for 100 cycles (0.275 ns + 2.525 ns) under the NVT ensemble at 300 K.

In AIMD, the Perdew–Burke–Ernzerhof (PBE) functional is employed to describe the electron exchange and correction energies within the generalized gradient approximation (GGA).<sup>44,45</sup> The projector augmented wave (PAW) method as implemented in VASP is used in this work.<sup>46</sup> Concerning the Brillouin zone integration, a 1 × 1 × 1 Monkhorst–Pack *k*-point mesh is chosen, and a 400 eV energy cutoff for plane-wave basis expansion.<sup>47</sup> To consider the London dispersion integrations, the Grimme D3 correction is also added. 0.2 eV and 10<sup>−4</sup> eV are utilized as the Gaussian smearing and threshold for electronic structure convergence.

HAIR simulation can provide the detailed reaction mechanism from the reactive trajectory in forming the primitive SEI. Fig. 1 exhibits FSI<sup>−</sup> and TTE decomposition details in the LiFSI/DME/TTE mixture observed from 0 to 11.5 ps HAIR simulations. The decomposition of TTE starts from LiF formation at around

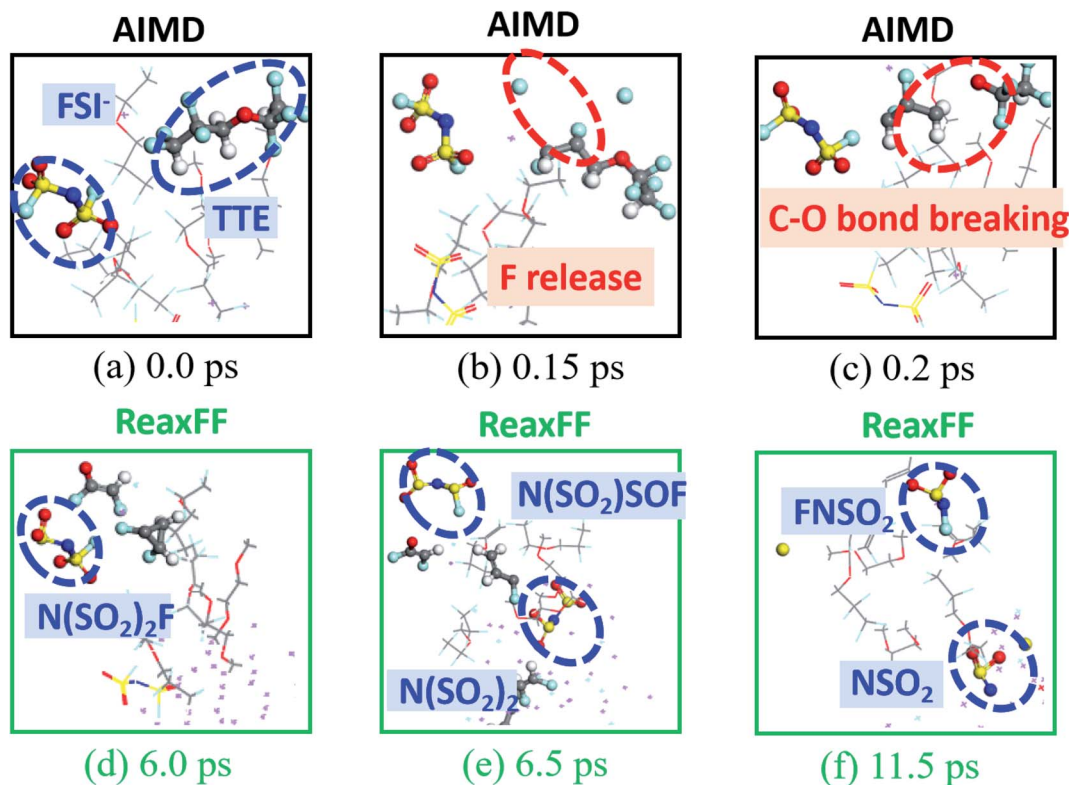


Fig. 1 The sequence of  $\text{FSI}^-$  and TTE decomposition obtained from HAIR simulations for the  $\text{LiFSI}/\text{DME}/\text{TTE}$  mixture between 0 and 11.5 ps. Black and green lines represent the AIMD and ReaxFF parts. The species are marked with blue, and reactions are marked with red. (a) 0.0, (b) 0.15, (c) 0.2, (d) 6.0, (e) 6.5, and (f) 11.5 ps. Color code: lithium, purple; oxygen, red; carbon, gray; fluorine, cyan; sulfur, yellow; nitrogen, blue; hydrogen, white.

0.15 ps. The C–O bond in TTE breaks *via* a reduction reaction with  $\text{Li}^0$  as reducing agent, leading to the formation of  $\text{LiOCF}_2\text{CF}_2\text{H}$  and  $\text{CFHCFCCH}_2$ . No decomposition of  $\text{FSI}^-$  is observed within 0.2 ps, which shows a slight difference from the previous salt decomposition process. Reduction of  $\text{FSI}^-$  creates  $\text{N}(\text{SO}_2)_2\text{F}$  *via* S–F bond cleavage after 6.0 ps. The following S–F bond breaking and N–S bond cleavage happen at 6.5 ps and 11.5 ps. Similar reductive reactions have been reported in our previous study of the  $\text{LiFSI}/\text{DOL}$  system,<sup>36</sup> in which all of the S–F bond breakings occur at 1.5 ps and the N–S bond breaks at around 5.6 ps, which is much earlier than those of the  $\text{LiFSI}/\text{DME}/\text{TTE}$  system. At approximately 11.5 ps, two  $\text{FSI}^-$  and three TTE molecules were reduced while the two DME molecules remained without undergoing any reactions in the  $\text{LiFSI}/\text{DME}/\text{TTE}$  mixture. Therefore, TTE can be more easily reduced than other species. The initial decomposition reactions of TTE are also validated by AIMD simulations within 20 ps, as shown in Fig. S2.†

The highest occupied molecular orbital (HOMO) and LUMO energy levels have been related to the oxidation–reduction potential. To further understand the original reactivity of species in the LHCE system, HOMO and LUMO energy levels are calculated, and the results are shown in Fig. 2. TTE exhibits the lowest LUMO (−0.58 eV) among the uncoordinated species such as DME (0.23 eV) and  $\text{FSI}^-$  ion (2.97 eV). The energy levels of TTE demonstrate a high electron affinity

according to the frontier molecular orbital theory,<sup>48,49</sup> which is prone to be reduced among other species in the electrolyte. As for the contact ion pairs (CIPs),  $\text{FSI}^-$  or DME is coordinated to  $\text{Li}^+$  ion in the inner solvation sheath, and the HOMO energies of the CIPs are lower than that of free salt and solvent molecules, which indicates that the CIP formation significantly improves the oxidative stability of electrolytes. Although the LUMO energy levels of CIPs are lowered by the coordination of  $\text{Li}^+$  ion, the LUMO orbitals of CIPs are located on  $\text{FSI}^-$  parts instead of DME, confirming that the  $\text{FSI}^-$  decomposes before DME. Thus, TTE and the  $\text{FSI}^-$  are firstly reduced due to the HOMO and LUMO energy levels of free molecules and CIPs, contributing to the formation of the SEI layer, agreeing well with experiments.<sup>27</sup>

As the simulation reactions continued, an interesting initiation of polymerization reaction of  $\text{OCH}=\text{C}(\text{NS})=\text{CH}_2$  and  $\text{CH}_2\text{CFC}(\text{H})\text{FC}(\text{CH})\text{CH}_2$  is traced from HAIR simulations. Fig. 3 shows the MD trajectories of polymerization during 61.0 and 215.0 ps. The unsaturated  $\text{OCH}=\text{C}=\text{CH}_2$ , which is formed by the C–F and C–O bond cleavages of TTE, is attacked by  $\text{S}\equiv\text{N}$  at the center carbon atom to generate  $\text{OCH}=\text{C}(\text{NS})=\text{CH}_2$  at 66.5 ps. Subsequently, the carbon skeleton ( $\text{CH}_2\text{CFC}(\text{H})\text{FC}(\text{CH})\text{CH}_2$ ), formed *via* releasing fluorine atoms from TTE, initiates the following polymerization process. At 82.0 ps, the recombination reaction occurs by  $\text{OCH}=\text{C}(\text{NS})=\text{CH}_2$  and  $\text{CH}_2\text{CFC}(\text{H})\text{FC}(\text{CH})\text{CH}_2$  as in Fig. 3(c). The following step is a ring-closure process,

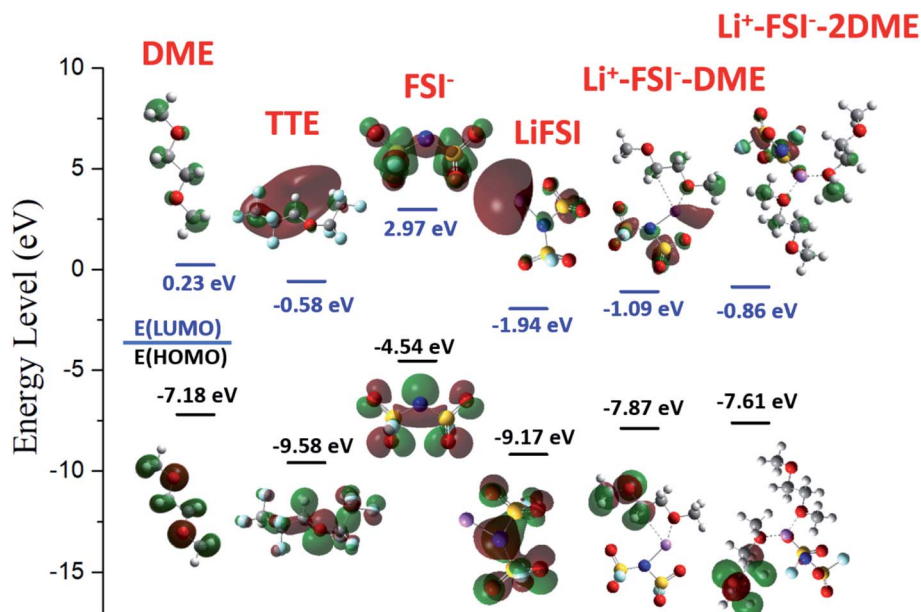


Fig. 2 The HOMO and LUMO orbitals and energies for DME, TTE, FSI<sup>-</sup>, LiFSI, Li<sup>+</sup>-FSI<sup>-</sup>, -DME, and Li<sup>+</sup>-FSI<sup>-</sup>-2DME contact ion pairs were obtained from DFT calculations. The red and green regions represent the positive and negative phases of the molecular orbitals, respectively. All molecular orbitals are shown with an iso value of 0.03.

in which the carbon atom in the terminal group attacks the unsaturated carbon atom to form a five-member ring, as shown in Fig. 3(d). HC=C=CHO attacks the circular molecule along

with bond breaking at 182.0 ps, and a subsequent ring-closure reaction is seen to form a six-member ring molecule (Fig. 3(f)). A similar polymerization process is also observed in configuration

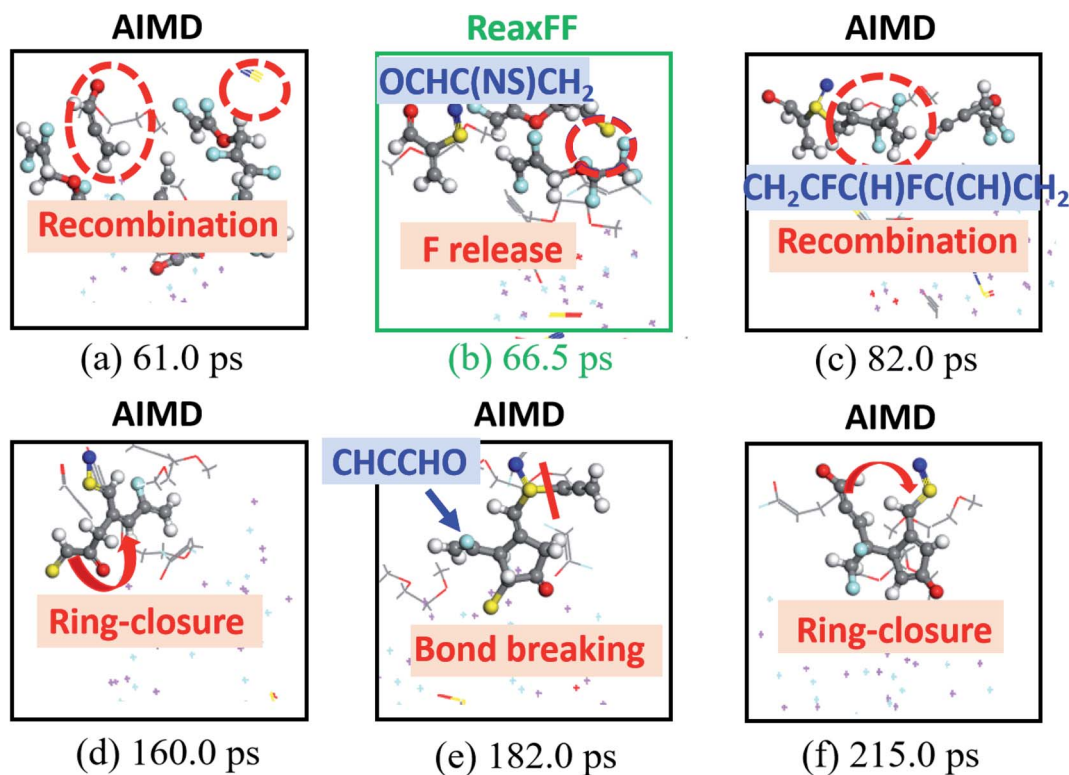


Fig. 3 The sequence of polymerization process obtained from HAIR simulations for the LiFSI/DME/TTE mixture between 61.0 and 215 ps. Black and green lines represent the AIMD and ReaxFF parts. The species are marked with blue and reaction processes are marked with red. (a) 61.0, (b) 66.5, (c) 82.0, (d) 160.0, (e) 182.0, and (f) 215.0 ps. The color codes are the same as in Fig. 1.



2, and the circular and branched types of the oligomers formed within 275 ps are exhibited in Fig. S3.†

After 50 cycles of initial reactions, the mass transfer process plays a dominant role in the following simulations. Thus, long-time MD simulations are performed with the HAIR method using a 100-time factor to accelerate the reductive reactions for another 50 cycles (2.525 ns). Fig. 4 shows the compositions and the morphological structure of the SEI layer generated in two configurations. Prominent organic and inorganic parts could be observed after long-time simulations. As shown in Fig. 4(a), the main component of the organic part is formed in the polymerization process owing to TTE decomposition, which is a circular-type organic product as shown in Fig. S3.† As for the inorganic component, the product of the homogeneous layer is LiF, mainly derived from the reductive reactions of TTE and  $\text{FSI}^-$  ion. In Fig. 4(b), long-chain type molecules of the organic part are formed in configuration 2, which undergoes a polymerization process as in configuration 1. No ring-closure reaction is observed within 2.8 ns simulations.

The polymerization is constrained within hundreds of atoms due to the simulation cell's small size, resulting in oligomers, which should evolve into bigger polymeric structures given a greater simulation size that is closer to experimental conditions. Realizing that existing simulations are limited to hundreds of atoms, nanoseconds, and just a few independent samples, more efficient methods, taking AIMD output as the training set, are under development by our group and other groups to advance battery modeling.

According to the reaction mechanism and SEI layer formation process observed in HAIR simulations, we can now rationalize the role of TTE in the SEI formation of LHCE systems. TTE exhibits a unique solution structure and unique reactivity in the reductive

reaction of electrolytes. The initial decomposition of TTE provides a fluorine atom, which contributes to the formation of the LiF inorganic layer in the SEI on account of the sufficient Li atoms, and the inorganic part shows a homogeneous morphological structure. In addition, after the initial defluorination reaction of TTE, the carbon skeleton offers a large number of unsaturated carbon atoms, initiating the polymerization process and further constructing the carbon framework. Consequently, the decomposition of TTE exhibits unexpected reactivity towards SEI formation *via* an *in situ* polymerization process, and the stable SEI layer, consisting of the organic oligomers and inorganic LiF parts, exhibits outstanding  $\text{Li}^+$  ion transport/transfer, electronic insulation, and mechanical properties.<sup>50</sup>

Radial distribution function (RDF) and X-ray photoelectron spectroscopy (XPS) are conducted to investigate the composition and structure of the SEI layer after 2.8 ns HAIR simulations. As shown in Fig. S4,† the peaks that appear at 1.5 Å and 2.0 Å could be attributed to C–C and Li–F bonds, respectively, indicating LiF and branched oligomer formation. To simulate the XPS spectra results, over 1000 structures are obtained from final AIMD simulations. The binding energies are calculated by initial state approximation using VASP at the PBE-D3 level, and statistical distributions are fitted with the Gaussian function.<sup>51,52</sup> Fig. 5 exhibits the simulated XPS result of configuration 1, and the experimental results are obtained from Ren's work.<sup>27</sup> The binding energy shift of C–F to Li–F is 2.7 eV, which is in good agreement with experimental values (2.6 eV), confirming LiF as the main component of the inorganic part in the SEI layer. For the organic part, the XPS signals indicate the presence of some carbon-based compounds, such as C–C/C–H, O–C–O, and C=O. The simulated results for configuration 2 are shown in Fig. S5,† and the exact values are listed in Tables S1–S3.†

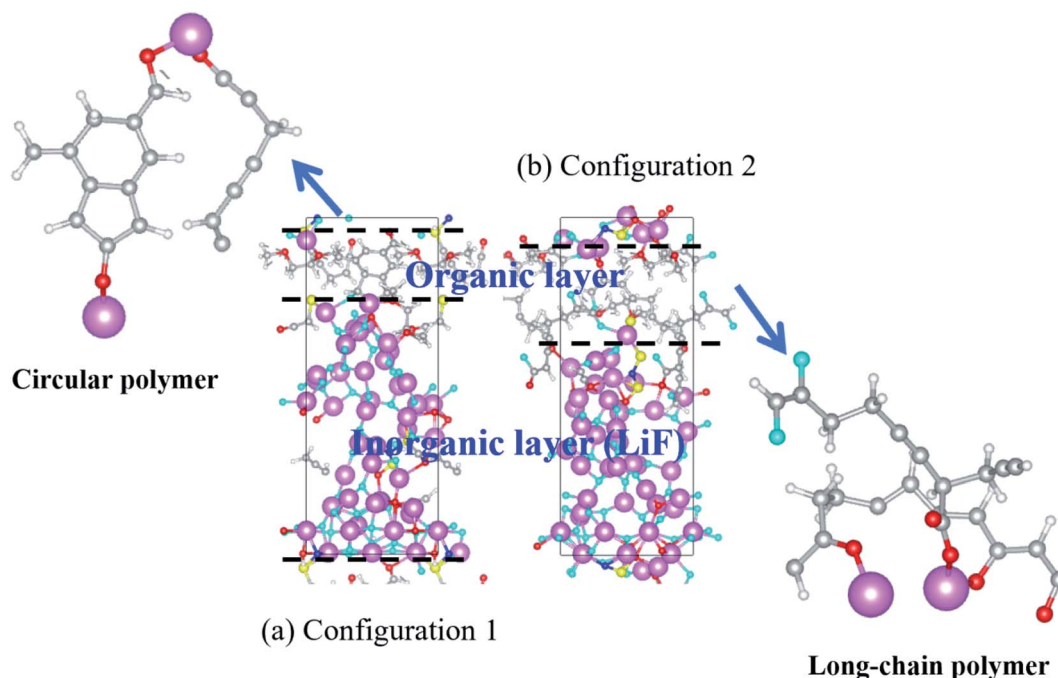


Fig. 4 Snapshots of long-time HAIR MD simulations (2.8 ns) for two configurations. The color codes are the same as in Fig. 1.

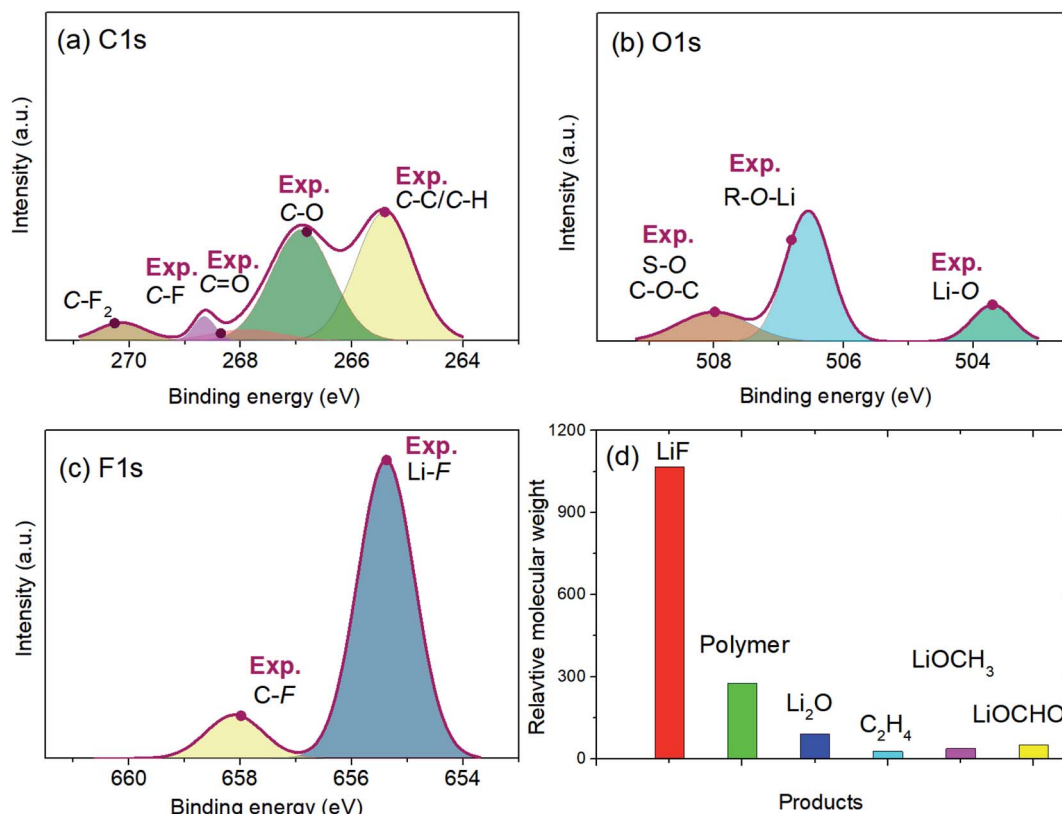


Fig. 5 XPS spectra of configuration 1 for (a) C 1s; (b) O 1s; and (c) F 1s. Wine red dots marked with Exp. represent the experimental binding energy shifts from ref. 25, and the corresponding values are shown in Tables S1–S3.† (d) is the relative molecular weight for the main products.

Current ReaxFF cannot distinguish homolytic bond breaking (HBB) and electron-coupled heterolytic bond breaking (eHBB), because it has no explicit description of electron. Because both of these reactions occur during the SEI formation, when ReaxFF fails, QM is a better option for simultaneously describing these reactions. With sufficient AIMD cycles, HAIR warrants the simulation accuracy compatibles with DFT, while reducing the cost by relying on ReaxFF. In this work, we focus on the initial reactions in forming a primitive SEI, when most of the reactions are quick chemical reactions that can be described in HAIR. The second stage SEI formation after primitive SEI occurs during charge/discharge cycles, an electrochemical reaction that involves electron transfer. These reactions are much slower than the initial reactions that require a technique beyond HAIR. A related technique to simulate the second stage SEI formation is under development.

In summary, a hybrid AIMD-ReaxFF scheme (HAIR) is employed to explore the reaction mechanism in the initial stage of the SEI formation process at the Li-metal anode of an LHCE system. The unique LHCE systems exhibit similar electrochemical performances to the HCE system. Meanwhile, LHCE solves the HCE system's drawbacks, such as high viscosity and cost. The model of the LHCE system consists of LiFSI and DME along with five TTE molecules as demonstrated in the experiments. According to the HAIR simulations, TTE and FSI<sup>−</sup> provide sufficient fluorine atoms to form LiF, which has been considered an excellent inorganic component of SEI. According

to the HOMO and LUMO energy levels, the LUMO of TTE and the FSI<sup>−</sup> ion in CIPs are much lower than other species, consistent with experimental and theoretical observations. Polymerization begins around 61.0 ps, and is triggered by TTE decomposition. Long-time simulations (2.8 ns) with a 100-time factor are used to speed mass transfer and further elucidate the SEI formation process. The morphological structure of the SEI layer exhibits distinct inorganic and organic regions, when both TTE and FSI<sup>−</sup> provide sufficient F<sup>−</sup> to form LiF, and the reduction product of TTE provides the backbone of oligomers. *In situ* polymerization of these unsaturated carbon backbones results in a carbon rich building framework in the organic component of the SEI layer. RDF and XPS spectra of SEI are employed to show good agreements with experiments. These theoretical findings show that the dilute solvent TTE plays an important role in the reductive reaction of LHCE on the Li-metal anode, providing fluorine-rich species and a carbon-based framework for the SEI layer's inorganic and organic components.

## Conflicts of interest

The authors declare no competing financial interests.

## Acknowledgements

T. C. is thankful for the support from the Collaborative Innovation Center of Suzhou Nano Science & Technology, the

Priority Academic Program Development of Jiangsu Higher Education Institutions (PAPD), the 111 Project, Joint International Research Laboratory of Carbon-Based Functional Materials and Devices, the National Natural Science Foundation of China (21903058 and 22173066), the Natural Science Foundation of Jiangsu Higher Education Institutions (BK20190810), and the Jiangsu Province High-Level Talents (JNHB-106).

## References

- 1 X. B. Cheng, R. Zhang, C. Z. Zhao and Q. Zhang, Toward Safe Lithium Metal Anode in Rechargeable Batteries: A Review, *Chem. Rev.*, 2017, **117**, 10403–10473.
- 2 J. B. Goodenough and K. S. Park, The Li-Ion Rechargeable Battery: A Perspective, *J. Am. Chem. Soc.*, 2013, **135**, 1167–1176.
- 3 B. Dunn, H. Kamath and J. M. Tarascon, Electrical Energy Storage for the Grid: A Battery of Choices, *Science*, 2011, **334**, 928–935.
- 4 W. Xu, J. Wang, F. Ding, X. Chen, E. Nasybulin, Y. Zhang and J. G. Zhang, Lithium Metal Anodes for Rechargeable Batteries, *Energy Environ. Sci.*, 2014, **7**, 513.
- 5 J. M. Zheng, M. H. Engelhard, D. H. Mei, S. H. Jiao, B. J. Polzin, J. G. Zhang and W. Xu, Electrolyte Additive Enabled Fast Charging and Stable Cycling Lithium Metal Batteries, *Nat. Energy*, 2017, **2**, 17012.
- 6 D. Lin, Y. Liu and Y. Cui, Reviving the Lithium Metal Anode for High-Energy Batteries, *Nat. Nanotechnol.*, 2017, **12**, 194–206.
- 7 F. Ding, W. Xu, X. Chen, J. Zhang, M. H. Engelhard, Y. Zhang, B. R. Johnson, J. V. Crum, T. A. Blake, X. Liu, *et al.*, Effects of Carbonate Solvents and Lithium Salts on Morphology and Coulombic Efficiency of Lithium Electrode, *J. Electrochem. Soc.*, 2013, **160**, A1894–A1901.
- 8 F. Shi, A. Pei, D. T. Boyle, J. Xie, X. Yu, X. Zhang and Y. Cui, Lithium Metal Stripping Beneath the Solid Electrolyte Interphase, *Proc. Natl. Acad. Sci. U.S.A.*, 2018, **115**, 8529–8534.
- 9 J. Scheers, S. Fantini and P. Johansson, A Review of Electrolytes for Lithium–Sulphur Batteries, *J. Power Sources*, 2014, **255**, 204–218.
- 10 C. Huang, J. Xiao, Y. Shao, J. Zheng, W. D. Bennett, D. Lu, L. V. Saraf, M. Engelhard, L. Ji, J. Zhang, *et al.*, Manipulating Surface Reactions in Lithium–Sulphur Batteries Using Hybrid Anode Structures, *Nat. Commun.*, 2014, **5**, 3015.
- 11 K. Xu, Electrolytes and Interphases in Li-ion Batteries and Beyond, *Chem. Rev.*, 2014, **114**, 11503–11618.
- 12 S. Li, M. Jiang, Y. Xie, H. Xu, J. Jia and J. Li, Developing High-Performance Lithium Metal Anode in Liquid Electrolytes: Challenges and Progress, *Adv. Mater.*, 2018, **30**, e1706375.
- 13 K. Ueno, K. Yoshida, M. Tsuchiya, N. Tachikawa, K. Dokko and M. Watanabe, Glyme–Lithium Salt Equimolar Molten Mixtures: Concentrated Solutions or Solvate Ionic Liquids?, *J. Phys. Chem. B*, 2012, **116**, 11323–11331.
- 14 Y. Jie, X. Ren, R. Cao, W. Cai and S. Jiao, Advanced Liquid Electrolytes for Rechargeable Li Metal Batteries, *Adv. Funct. Mater.*, 2020, **30**, 1910777.
- 15 C. Wang, K. Fu, S. P. Kammampata, D. W. McOwen, A. J. Samson, L. Zhang, G. T. Hitz, A. M. Nolan, E. D. Wachsman, Y. Mo, *et al.*, Garnet-Type Solid-State Electrolytes: Materials, Interfaces, and Batteries, *Chem. Rev.*, 2020, **120**, 4257–4300.
- 16 C. Wu, F. Guo, L. Zhuang, X. Ai, F. Zhong, H. Yang and J. Qian, Mesoporous Silica Reinforced Hybrid Polymer Artificial Layer for High-Energy and Long-Cycling Lithium Metal Batteries, *ACS Energy Lett.*, 2020, **5**, 1644–1652.
- 17 X. B. Cheng, R. Zhang, C. Z. Zhao, F. Wei, J. G. Zhang and Q. Zhang, A Review of Solid Electrolyte Interphases on Lithium Metal Anode, *Adv. Sci.*, 2016, **3**, 1500213.
- 18 J. Holoubek, H. Liu, Z. Wu, Y. Yin, X. Xing, G. Cai, S. Yu, H. Zhou, T. A. Pascal, Z. Chen and P. Liu, Tailoring Electrolyte solvation for Li Metal Batteries Cycled at Ultra-Low Temperature, *Nat. Energy*, 2021, **6**, 303–313.
- 19 Y. Yamada, M. Yaegashi, T. Abe and A. Yamada, A Super-Concentrated Ether Electrolyte for Fast-Charging Li-Ion Batteries, *Chem. Commun.*, 2013, **49**, 11194–11196.
- 20 L. Suo, Y. S. Hu, H. Li, M. Armand and L. Chen, A New Class of Solvent-in-Salt Electrolyte for High-Energy Rechargeable Metallic Lithium Batteries, *Nat. Commun.*, 2013, **4**, 1481.
- 21 J. F. Qian, W. A. Henderson, W. Xu, P. Bhattacharya, M. Engelhard, O. Borodin and J. G. Zhang, High Rate and Stable Cycling of Lithium Metal Anode, *Nat. Commun.*, 2015, **6**, 6362.
- 22 Y. Yamada, K. Furukawa, K. Sodeyama, K. Kikuchi, M. Yaegashi, Y. Tateyama and A. Yamada, Unusual Stability of Acetonitrile-Based Superconcentrated Electrolytes for Fast-Charging Lithium-Ion Batteries, *J. Am. Chem. Soc.*, 2014, **136**, 5039–5046.
- 23 S. Chen, S. Zheng, D. Mei, K. S. Han, M. H. Engelhard, W. Zhao, W. Xu, J. Liu and J. G. Zhang, High-Voltage Lithium-Metal Batteries Enabled by Localized High Concentration Electrolytes, *Adv. Mater.*, 2018, **30**, e1706102.
- 24 X. Ren, S. Chen, L. Hongkyung, D. Mei, M. H. Engelhard, S. D. Burton, W. Zhao, J. Zheng, Q. Li and M. S. Ding, Localized High-Concentration Sulfone Electrolytes for High-Efficiency Lithium-Metal Batteries, *Chem*, 2018, **4**, 1877–1892.
- 25 X. Ren, L. F. Zou, X. Cao, M. H. Engelhard, W. Liu, S. D. Burton, L. Hongkyung, C. J. Niu, B. E. Matthews, Z. H. Zhu, C. M. Wang, B. W. Arey, J. Xiao, J. Liu, J. G. Zhang and W. Xu, Enabling High-Voltage Lithium-Metal Batteries under Practical Conditions, *Joule*, 2019, **3**, 1662–1676.
- 26 H. Liu, J. Holoubek, H. Zhou, A. Chen, N. Chang, Z. Wu, S. Yu, Q. Yan, X. Xing, Y. Li, T. A. Pascal and P. Liu, Ultrahigh Coulombic Efficiency Electrolyte Enables Li||SPAN Batteries with Superior Cycling Performance, *Mater. Today*, 2021, **42**, 17–28.
- 27 X. Ren, P. Y. Gao, L. F. Zou, S. H. Jiao, X. Cao, X. H. Zhang, H. Jia, M. H. Engelhard, B. E. Matthews, H. P. Wu, L. Hongkyung, C. J. Niu, C. M. Wang, B. W. Arey, J. Xiao, J. Liu, J. G. Zhang and W. Xu, Role of Inner Solvation Sheath Within Salt–Solvent Complexes in Tailoring Electrode/Electrolyte Interphases for Lithium Metal

- Batteries, *Proc. Natl. Acad. Sci. U.S.A.*, 2020, **117**(46), 28603–28613.
- 28 A. Wang, S. Kadam, L. Li, S. Shi and Y. Qi, Review on Modeling of the Anode Solid Electrolyte Interphase (SEI) for Lithium-Ion Batteries, *Npj Comput. Mater.*, 2018, **4**, 15.
- 29 E. P. Kamphaus, S. Angarita-Gomez, X. Qin, M. Shao, M. Engelhard, K. T. Mueller, V. Murugesan and P. B. Balbuena, Role of Inorganic Surface Layer on Solid Electrolyte Interphase Evolution at Li-Metal Anodes, *ACS Appl. Mater. Interfaces*, 2019, **11**, 31467–31476.
- 30 S. Q. Shi, J. Gao, Y. Liu, Y. Zhao, Q. Wu, W. J. Wang, C. Y. Ouyang and R. J. Xiao, Multi-Scale Computation Methods: Their Applications in Lithium-Ion Battery Research and Development, *Chin. Phys. B*, 2016, **25**, 018212.
- 31 S. P. Beltran, X. Cao, J. G. Zhang and P. B. Balbuena, Localized High Concentration Electrolytes for High Voltage Lithium-Metal Batteries: Correlation between the Electrolyte Composition and Its Reductive/Oxidative Stability, *Chem. Mater.*, 2020, **32**, 5973–5984.
- 32 Y. Zheng, F. A. Soto, V. Ponce, J. M. Seminario, X. Cao, J. G. Zhang and P. B. Balbuena, Localized High Concentration Electrolyte Behavior near a Lithium-Metal Anode Surface, *J. Mater. Chem.*, 2019, **7**, 25047–25055.
- 33 K. Leung and J. L. Budzien, *Ab initio* Molecular Dynamics Simulations of the Initial Stages of Solid-Electrolyte Interphase Formation on Lithium Ion Battery Graphitic Anodes, *Phys. Chem. Chem. Phys.*, 2010, **12**, 6583–6586.
- 34 J. M. Martinez de la Hoz, K. Leung and P. B. Balbuena, Reduction Mechanisms of Ethylene Carbonate on Si Anodes of Lithium-Ion Batteries: Effects of Degree of Lithiation and Nature of Exposed Surface, *ACS Appl. Mater. Interfaces*, 2013, **5**, 13457–13465.
- 35 Y. Liu, P. Yu, Y. Wu, H. Yang, M. Xie, L. Huai, W. A. Goddard and T. Cheng, The DFT-ReaxFF Hybrid Reactive Dynamics Method with Application to the Reductive Decomposition Reaction of the TFSI and DOL Electrolyte at a Lithium-Metal Anode Surface, *J. Phys. Chem. Lett.*, 2021, **12**, 1300–1306.
- 36 Y. Liu, P. Yu, Q. Sun, P. Yu, Y. Wu, L. Xu, H. Yang, M. Xie, T. Cheng and W. A. Goddard, Effects of High and Low Salt Concentrations in Electrolytes at Lithium-Metal Anode Surfaces Using DFT-ReaxFF Hybrid Molecular Dynamics Method, *J. Phys. Chem. Lett.*, 2021, **12**, 2922–2929.
- 37 M. Xie, Y. Wu, Y. Liu, P. P. Yu, R. Jia, W. A. Goddard III and T. Cheng, Pathway of *in situ* Polymerization of 1,3-Dioxolane in LiPF<sub>6</sub> Electrolyte on Li Metal Anode, *Mater. Today Energy*, 2021, **21**, 100730.
- 38 Y. Liu, Q. Sun, Y. Wu, M. Xie, H. Yang, T. Cheng and W. A. Goddard, Predicted Operando Polymerization at Lithium Anode via Boron Insertion, *ACS Energy Lett.*, 2021, **6**, 2320–2327.
- 39 D. Bedrov, G. D. Smith and A. C. T. van Duin, Reactions of Singly-Reduced Ethylene Carbonate in Lithium Battery Electrolytes: A Molecular Dynamics Simulation Study Using the ReaxFF, *J. Phys. Chem. A*, 2012, **116**, 2978–2985.
- 40 L. E. Camacho-Forero, T. W. Smith, S. Bertolini and P. B. Balbuena, Reactivity at the Lithium-Metal Anode Surface of Lithium–Sulfur Batteries, *J. Phys. Chem. C*, 2015, **119**, 26828–26839.
- 41 L. E. Camacho-Forero and P. B. Balbuena, Effects of Charged Interfaces on Electrolyte Decomposition at the Lithium Metal Anode, *J. Power Sources*, 2020, **472**, 228449.
- 42 G. Kresse and J. Hafner, *Ab initio* Molecular-Dynamics Simulation of the Liquid-Metamorphous-Semiconductor Transition Germanium, *Phys. Rev. B: Condens. Matter Mater. Phys.*, 1994, **49**(20), 14251–14269.
- 43 S. Plimpton, Fast Parallel Algorithms for Short-Range Molecular Dynamics, *J. Comput. Phys.*, 1995, **117**, 1–19.
- 44 J. P. Perdew, K. Burke and M. Ernzerhof, Generalized Gradient Approximation Made Simple, *Phys. Rev. Lett.*, 1996, **77**(18), 3865–3868.
- 45 S. Naserifar, J. J. Oppenheim, H. Yang, T. Zhou, S. Zybin, M. Rizk and W. A. Goddard, Accurate Non-Bonded Potentials Based on Periodic Quantum Mechanics Calculations for Use in Molecular Simulations of Materials and Systems, *J. Chem. Phys.*, 2019, **151**, 154111.
- 46 G. Kresse and D. Joubert, From ultrasoft pseudopotentials to the projector augmented-wave method, *Phys. Rev. B: Condens. Matter Mater. Phys.*, 1999, **59**(3), 1758–1775.
- 47 H. J. Monkhorst and J. D. Pack, Special Points for Brillouin-Zone Integrations, *Phys. Rev. B*, 1976, **13**(12), 5188–5192.
- 48 W. D. Zhang, S. Q. Zhang, L. Fan, L. Gao, X. Q. Kong, S. Y. Li, J. Li, X. Hong and Y. Y. Lu, Tuning the LUMO Energy of an Organic Interphase to Stabilize Lithium Metal Batteries, *ACS Energy Lett.*, 2019, **4**, 644–650.
- 49 X. Cao, H. Jia, W. Xu and J. G. Zhang, Review—Localized High-Concentration Electrolytes for Lithium Batteries, *J. Electrochem. Soc.*, 2021, **168**, 010522.
- 50 Y. B. Zhao, Y. Bai, W. D. Li, M. Z. An, Y. P. Bai and G. R. Chen, Design Strategies for Polymer Electrolytes with Ether and Carbonate Groups for Solid-State Lithium Metal Batteries, *Chem. Mater.*, 2020, **32**(16), 6811–6830.
- 51 L. Köhler and G. Kresse, Density Functional Study of CO on Rh(111), *Phys. Rev. B: Condens. Matter Mater. Phys.*, 2004, **70**, 165405.
- 52 J. Qian, A. Baskin, Z. Liu, D. Prendergast and E. J. Crumlin, Addressing the Sensitivity of Signals from Solid/Liquid Ambient Pressure XPS (APXPS) Measurement, *J. Chem. Phys.*, 2020, **153**, 044709.